



Highly efficient visible light driven photocatalytic inactivation of *E. coli* with Ag QDs decorated Z-scheme Bi₂S₃/SnIn₄S₈ composite



Huanxian Shi^a, Cunjin Wang^a, Yanyan Zhao^a, Enzhou Liu^a, Jun Fan^{b,*}, Zhen Ji^{c,*}

^a School of Chemical Engineering, Northwest University, Xi'an, 710069, PR China

^b College of Food Science and Engineering, Northwest University, Xi'an 710069, PR China

^c Faculty of Chemistry and Chemical Engineering, Ankang University, Ankang 725000, PR China

ARTICLE INFO

Keywords:

Photocatalytic disinfection
Ag QDs/Bi₂S₃/SnIn₄S₈ composite
Z-Scheme mechanism
Surface plasma resonance (SPR)

ABSTRACT

Here, a novel Ag QDs modified Bi₂S₃/SnIn₄S₈ composite with direct Z-scheme charge carriers transfer model was synthesized through combining with chemical reduction and solvothermal methods for high-efficient photodisinfection toward *E. coli* under visible light stimulation ($\lambda > 420$ nm). The 200 Ag QDs/Bi₂S₃/SnIn₄S₈ hybrid exhibited the strongest photocatalytic inactivation activity of *E. coli* which could completely inactivate the bacteria with 4 h visible light excitation. The photoactivation mechanism can be ascribed to the wreck of cell membrane, leakage and damage of intracellular biomolecules including protein and DNA as demonstrated by fluorescence-based live/dead stain, sodium dodecyl sulfate polyacrylamide gel electrophoresis (SDS-PAGE) and agarose gel electrophoresis (AGE). Moreover, the trapping and verification experiments of free radical revealed that the reactive species h⁺, e⁻ and ·O₂ play the chief role in photodisinfection reaction. The photoelectrochemical techniques disclosed that the enhanced photocatalytic activity could mainly be assigned to the synergistic effect of Ag QDs, Bi₂S₃ and SnIn₄S₈, which could improve the visible light absorption ability, separation and transfer efficiency of photoinduced charge carriers, enlarge specific surface area through the surface plasma resonance (SPR) effect and the electron trapped and injected of Ag QDs. Additionally, the Ag QDs/Bi₂S₃/SnIn₄S₈ composite displayed a potential application in organic contaminant removal. Our work firmly exhibited a promising environmental friendly substitutable strategy for wastewater purification caused by pathogenic bacteria and organic pollutant.

1. Introduction

Water is the precious and indispensable resource in our daily life. Unfortunately, in the past decades, water pollution caused by pathogenic microorganisms has posed overwhelming threat to environmental safe and human health [1,2]. However, the conventional water disinfection strategies such as ultraviolet radiation, chlorination, ozonation, filtration technology have exhibited several drawbacks linked to the potential disinfection byproducts (DBPs) and costly-operation [3–5]. Therefore, developing a cost-efficient, environmental friendly and reliable water purification technique has become the essential issue. Contrast to the orthodox approach, photocatalytic disinfection technology has attracted escalating concerns because its unprecedented advantage of without disinfection byproducts generation during the bactericidal process. Since Matsunaga et al. revealed the TiO₂ photocatalyst possessed the ability of inactivation bacteria through generating reactive oxygen species (ROS) including h⁺, e⁻, ·OH and ·O₂−

under ultraviolet light excitation in 1985 [6], tremendous efforts have been devoted to exploring the high-efficient TiO₂-base photo-activated disinfection photocatalyst. Nevertheless, the practical application of TiO₂ was strictly restricted by the main disadvantages only respond to UV-region and rapid recombination of charge carriers [7–10]. Hence, designing and empoldering an innovative visible light driven photocatalyst for aquatic microbial disinfection has become the attractive hot-pot in term of employing the solar energy.

Recently, SnIn₄S₈ has attracted tremendous interesting because its superior photoelectric properties and relative narrow band energy (1.77–2.35 eV), and has exhibited versatile application in the domain of photovoltaic [11], photocatalysis [12–15]. However, the photocatalytic activity of bare SnIn₄S₈ is far from practical application for the repaid recombination of charge carriers. Therefore, it is a significant task for us to polish up the photocatalytic performance of SnIn₄S₈ for photocatalytic disinfection. To date, many approaches have been attempted to promote the photocatalytic activity of single catalyst such as metal

* Corresponding authors.

E-mail addresses: fanjun@nwu.edu.cn (J. Fan), jizhen@aku.edu.cn (Z. Ji).

doping [16,17], morphology tune [18,19], constructing heterojunction with two composites [17,20–22]. Among them, constructing heterojunction has been regarded as the promising strategy to ameliorate the photocatalytic performance of simplex catalyst. In particular, at present, constructing Z-scheme heterostructure has received progressively attention for its unique charge carriers transfer model. Different from the conventional double-transfer heterojunction whose redox ability of photogenerated electrons and holes were weaken during the transfer process, in Z-scheme transfer pathway, not only the separation efficiency of charge carriers is significantly promoted but also the strong redox capacity of the photoinduced holes and electrons are retained, which resulted in enhanced photocatalytic activity [23–26]. To date, numerous of Z-scheme heterostructures have been successfully prepared and exhibited diverse potential application in the sphere of environmental remediation and energy conversion, such as Z-Scheme SrTiO₃/La, Rh/C/BiVO₄:Mo [24], Z-scheme g-C₃N₄/m-Bi₂O₄ [25], Z-Scheme ZnO/CeO₂ [26] and so on. These motivate us to attempt to fabricate a novel SnIn₄S₈-base Z-scheme heterojunction photocatalyst for water disinfection.

Moreover, in many Z-scheme systems, the noble metal (Ag, Au, Pt, etc) played a significant role in maximizing the photocatalytic activity due to versatile functions such as acted as an electron mediator to conduct charge or served as sink of the charge carriers to promote the separation of charge carriers, enhance the absorption ability of visible light by the local surface plasmon resonance (SPR) effect [27–30]. For instance, Chen et al. proposed that the Ag nanoparticles in the Ag/P-C₃N₄/BiVO₄ composite can serve as the charge mediator and enhanced photodegradation ciprofloxacin activity [31]. In Ag/WO₃/Bi₂WO₆ system reported by Zhou. et al, the metal Ag can act as the electron injector and extremely boost the photocatalytic activity [32]. In the MoS₂/Ag dots/Ag₃PO₄ hybrids, the Ag served as recombination centers and promote the photocatalytic performance of MoS₂/Ag dots/Ag₃PO₄ for oxygen production [33]. The Ag in the Ag/Fe₃O₄/g-C₃N₄ composite functioned as the charge storage and enhance the photocatalytic activity [34]. The above reasons for the Z-scheme charge transfer pathway containing metal Ag with promoted photocatalytic performance may help us to design and fabricate a novel ternary containing silver SnIn₄S₈-base Z-scheme heterojunction and to illustrate the contribution of the Ag for the enhanced photocatalytic activity.

Herein, an innovative ternary Ag quantum dots (QDs) /Bi₂S₃/SnIn₄S₈ Z-Scheme heterostructure with a SPR effect was synthesized through the facile chemical reduction and solvothermal method for photodisinfection under visible light illumination ($\lambda > 420$ nm). The original Ag QDs/Bi₂S₃/SnIn₄S₈ heterojunctions displayed excellent photocatalytic disinfection performance towards *E.coli* superior to pure SnIn₄S₈ and Bi₂S₃/SnIn₄S₈ hybrid, which could absolutely inactivate the *E.coli* within 4 h visible light excitation. Besides, the photocatalytic inactivation effect and mechanism were in-depth investigated with diverse techniques including SEM, fluorescence-base dead/live stain, DNA and protein electrophoresis. The enhanced photocatalytic disinfection activity of Ag QDs/Bi₂S₃/SnIn₄S₈ heterojunctions could be ascribed to follow reasons: (1) binary Z-scheme heterojunction was formed between Bi₂S₃ and SnIn₄S₈ which favored for the separation efficiency of photogenerated charge carries; (2) improved visible light absorb ability and separation of charge carriers by the SPR effect of Ag QDs; (3) enlarged specific surface area after the introduction of the small size of Ag QDs.

2. Experiment section

2.1. Fabrication of sample

2.1.1. Preparation of Ag quantum dots (QDs)

All agents are analytical grade and employed without further purification. Ag QDs were fabricated according to the Di et al reported [16]. 2 mM AgNO₃ was dissolved in the mixture solution containing

20 mL Oleamine and 0.4 mL oleic acid. Then, the mixture solution was transferred into 100 mL autoclave and maintained at 120 °C for 18 h. After the autoclave was cooled down to surround temperature, the resultant suspension was precipitated by 30 mL acetone. Afterwards, the precipitate was washed with ethanol and redispersed in 20 mL n-hexane.

2.1.2. Preparation of Ag QDs /Bi₂S₃/ SnIn₄S₈ composites

Ag QDs/Bi₂S₃/SnIn₄S₈ heterojunctions were prepared through a simple solvothermal method. Different volume (50 μL, 100 μL, 2000 μL, 300 μL, 400 μL) of Ag QDs suspension were respectively added to the mixture precursor solution of Bi₂S₃/SnIn₄S₈ under magnetically stirred for 6 h. Then, the mixture solution was placed in a 100 mL autoclave and kept at 180°C for 12 h, after the autoclave was cooled down to room temperature, the precipitate was washed with absolutely ethanol and DI water. Then dried at 70°C for 12 h in a vacuum oven. The obtained samples were labeled as 50 Ag QDs/Bi₂S₃/SnIn₄S₈, 100 Ag QDs/Bi₂S₃/SnIn₄S₈, 200 Ag QDs/Bi₂S₃/SnIn₄S₈, 300 Ag QDs/Bi₂S₃/SnIn₄S₈, 400 AgQDs/Bi₂S₃/SnIn₄S₈, respectively. For comparison, the 2.5% Bi₂S₃/SnIn₄S₈ composite was synthesized as described in our previous report [14] without addition of Ag QDs suspension and labeled as Bi₂S₃/SnIn₄S₈.

2.2. Characterization

The crystal phase of the photocatalysts were collected from a Shimadzu XRD 6000 powder diffractometer with Cu Kα radiation ($\lambda = 0.1542$ Å). The morphology and microstructure of the samples were investigated by a Scanning electron microscope (SEM, Carl Zeiss SIGMA) equipped with energy dispersive spectrometry (EDS) and Tecnai G2 F20 S-TWIN transmission electronmicroscopy (TEM), respectively. The optical property of the products was determined by a 3600 UV-vis-NIR spectrophotometer (Shimadzu, Japan). X-ray photoelectron spectroscopy (XPS) was used to analysis the surface chemical states of the elements in catalysts. The photoluminescence (PL) emission spectra for solid samples were assayed utilizing Hitachi F-7000 fluorescence spectrometer. The photoelectric properties of the catalysts were characterized with CHI660E electrochemical workstation with standard three-electrode cell. Brunauer-Emmett-Teller (BET) surface area of the products was conducted with Quantachrome NOVA2000e at N₂ temperature 77 K.

2.3. Photocatalytic antibacterial activity evaluation

Gram-negative *Escherichia coli* (*E.coli*, ATCC25922) was selected as the model microbe to estimate the photoinactivation activity of the samples. Before the photodisinfection experiment, all glassware used here were sterilized at 121°C for 30 min, and the bactericidal experiments were conducted at aseptic condition. For photocatalytic disinfection, A beaker 50 mL reaction suspension containing 30 mg catalyst and *E. coli* cells (initial concentration: 2.5×10^7 cfu/mL) was irradiation under 300 W Xe lamp with a cutoff filter ($\lambda > 420$ nm). After certain time intervals, 0.5 mL of suspension was withdraw and diluted with sterilized saline by decimal method. Finally, an aliquot of the diluted solution was evenly dispersed on the Luria-Bertani (LB) solid medium and incubated at 37 °C for 24 h. The photodisinfection effect of catalyst was analysis by counting the colony-forming units (cfu) number of *E. coli* and expressed as log cfu/mL. Besides, the blank group was conducted without any photocatalyst.

2.4. Fluorescent-base cell live/dead analysis

To illustrate the time-evaluation disinfection effect of the samples on the *E.coli*, the fluorescent-base Cell Live/Dead stain was conducted. Typically, at given time intervals, an aliquot of the reaction suspension was withdraw and stained with mixture dye of Acridine orange/

ethidium bromide (AO/EB, Live/dead Baclight Bacterial Viability Kit, ST102, Hat Biotech, Xi'an, China) obeyed by the specification. The images were visualized with a fluorescent microscopy (Olympus, IX-53, Japan).

2.5. Total protein and DNA analysis of *E. coli*

To further reveal the leakage and damage of the intracellular content (total protein and DNA) in the photoactivation system. The total protein was extracted by the *E. coli* total protein extraction Kit (BB-3128, Bestbio, Shanghai, China), thereafter, determined with the BCA Elisa Kit (P0010S, Beyotime Biotech, Shanghai, China) and the 12% sodium dodecyl sulfate polyacrylamide gel electrophoresis (SDS-PAGE) at 120 V in Tris-Glycine SDS running buffer. The DNA was extracted according to the instruction of Ezup Column Bacteria Genomic DNA Purification Kit (SK8255, Sangon Biotech, Shanghai, China), then demonstrated with the 1% AGE at 100 V in 1 × TAE buffer. The Specific steps of electrophoresis of agarose gel (AGE) and SDS-PAGE gel were described in S1.

2.6. Photocatalytic degradation of RhB

To further evaluate the photocatalytic activity and explore the potential application of the as-fabricated products, Rhodamine B (RhB) was used to evaluate the photocatalytic degradation organic pollutant in aqueous solution. Briefly, A 300 W Xe lamp equipped with a UV cutoff filter ($\lambda > 420$ nm) was employed as the light source. Briefly, 10 mg catalyst was added into 50 mL RhB solution (10 mg/L) under continuously stirred. Before illumination, the reaction suspension was placed in dark under ceaselessly agitating for 60 min to achieve the zero point of adsorption. The concentration of RhB was monitored with the UV-vis spectrophotometer at the defined time intervals.

3. Results and discussion

3.1. Morphologic, structural and compositional information

The crystalline phase of the SnIn₄S₈, Ag QDs/SnIn₄S₈, Bi₂S₃/SnIn₄S₈, 200 Ag QDs/Bi₂S₃/SnIn₄S₈ composite were investigated by XRD. As shown in Fig. 1, the position of diffraction peaks of the pure SnIn₄S₈ were perfectly indexed to the cubic phase structure of SnIn₄S₈ (PDF#42-1305) [14]. Besides, there no impurity peaks existed on the pattern, indicating the high purity of the pure SnIn₄S₈. For other composites, except the diffraction peaks of SnIn₄S₈, the characteristic peak of Ag QDs and Bi₂S₃ could not be observed, which may be due to the mass of Ag QDs and Bi₂S₃ was not enough to be detected.

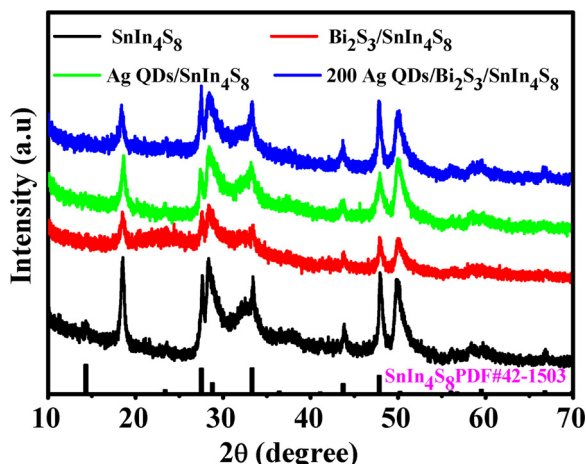


Fig. 1. The XRD patterns of the as-prepared samples.

SEM and TEM were respectively employed to observe the morphology and microstructure of SnIn₄S₈, Bi₂S₃/SnIn₄S₈, 200 Ag QDs/Bi₂S₃/SnIn₄S₈ hybrid. As Fig.S1a displays, the pure SnIn₄S₈ constructed with several disorder nanosheets. For Bi₂S₃/SnIn₄S₈ (Fig.S1b) and Ag QDs/Bi₂S₃/SnIn₄S₈ composite (Fig. 2a), they presented flower-like shape built with several nanoplates. The TEM (Fig. 2b) showed that the Ag QDs was successfully prepared and evenly dispersed with a diameter from 3.1~10 nm and the HRTEM (Fig. 2d) displayed the interplanar spacing 0.3269 nm was assigned to the (111) plane of Ag. In Fig. 2c, it can obviously observe that the Ag QDs, Bi₂S₃ and SnIn₄S₈ were perfectly coexisted in the Ag QDs/ Bi₂S₃/SnIn₄S₈ composite and the HRTEM revealed the lattice spacing 0.3527 nm and 0.2198 nm were attributed to (310) plane of Bi₂S₃ and (422) plane of SnIn₄S₈ (Fig.2e), respectively. Moreover, the EDS (Fig. 2f) image and elemental mapping (Fig.S1c-g) revealed that Bi, Ag, S, Sn, In elements were homogeneously dispersed in the Ag QDs/Bi₂S₃/SnIn₄S₈ composite.

XPS was applied to analyse the element composition and valence states of the SnIn₄S₈, Bi₂S₃/SnIn₄S₈, 200 Ag QDs/Bi₂S₃/SnIn₄S₈ composite. The survey spectra (Fig. 3a) evidently exhibited that the composite consist of S, In, Sn, Bi and Ag elements. To further reveal the chemical state of the each element in 200 Ag QDs/Bi₂S₃/SnIn₄S₈ composite, the high resolution XPS was employed. In Fig. 3b, the two peaks located at the binding energies of 487.1 eV and 495.5 eV were attributed to the Sn 3d_{5/2} and Sn 3d_{3/2}, respectively [35]. In Fig. 3c, the two characteristic peaks centered at 158.7 eV and 164.1 eV were match well with the Bi 4f_{7/2} and Bi 4f_{5/2}, respectively [36]. As shown in Fig. 3d, the binding energies of 445.0 eV and 452.5 eV, corresponding to the In 3d_{5/2} and In 3d_{3/2}, respectively [13]. In S 2p spectrum (Fig. 3e), the peak could be deconvoluted into two peaks which binding energies lied in 161.2 eV and 163.2 eV were indexed to the S 2p_{1/2} and S 2p_{3/2}, respectively [14,15]. Moreover, as Fig. 3f shows, the two peaks seated at 368.5 eV and 374.3 eV were assigned to the Ag 3d_{5/2} and Ag 3d_{3/2} of metal Ag⁰ [37,38]. Additionally, compared with the pure SnIn₄S₈ and Bi₂S₃, the binding energies of elements Sn, Bi, S in the 200 Ag QDs/Bi₂S₃/SnIn₄S₈ composite were slightly drifted to high energy spectrum, while the binding energy peaks slightly shifted to the direction of low energy in the In XPS spectrum, which could be attributed to the violent interaction was occurred during the synthesized process. The above results demonstrated that the Ag QDs/Bi₂S₃/SnIn₄S₈ composite was successfully fabricated by our strategies.

3.2. Photodisinfection towards *E. coli*

The photodisinfection performance of as-prepared products was evaluated by selecting the *E. coli* as the target microbe under visible light irradiation ($\lambda > 420$ nm). The inherent antibacterial activity of the samples was measured in the dark. As shown in Fig. 4a, in the presence of catalysts, the cell number almost remained the initial bacterial population, indicating the toxicity of the catalysts could be neglected which can be further verified by the not enlarged inhibition zone in the dark (Fig. S2). Besides, the affect of the visible light on the viability of the bacteria could also be ignored for the almost constant bacterial density within 4 h exposed to light (Fig. 4b). Under visible light irradiation, all catalysts displayed certain inactivation activity within 4 h visible light stimulation (Fig. 4b). For pure SnIn₄S₈, the 4.1- \log_{10} cfu/mL reduction of *E. coli* cells was achieved and approximately 5.1- \log_{10} cfu/mL decrease of *E. coli* population was obtained. Strikingly, the *E. coli* cell number was markedly reduced after the introduction of Ag QDs and the inactivation effect of the catalysts was firstly increased and then decreased with the volume of Ag QDs ascended. In particular, the 200 Ag QDs/Bi₂S₃/SnIn₄S₈ composite exhibited strongest inactivation effect on the *E. coli* which could absolutely inactivate the *E. coli* within 4 h under visible light excitation. However, when the volume of Ag QDs over 200 μ L, the reduction of the bactericidal property may be ascribed to the formation of recombination centre of photo-generated hole-electron pairs or formed the “shielding effect” by the

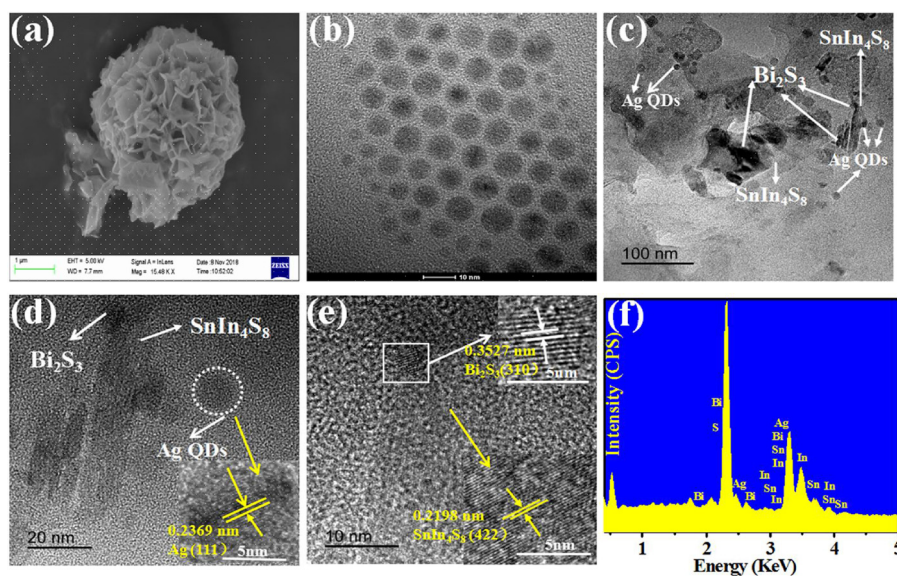


Fig. 2. (a) SEM of 200 Ag QDs/ Bi_2S_3 / SnIn_4S_8 , TEM of Ag QDs (b), 200 Ag QDs/ Bi_2S_3 / SnIn_4S_8 (c–d), HRTEM (e) and EDS spectra (f) of 200 AgQDs/ Bi_2S_3 / SnIn_4S_8 .

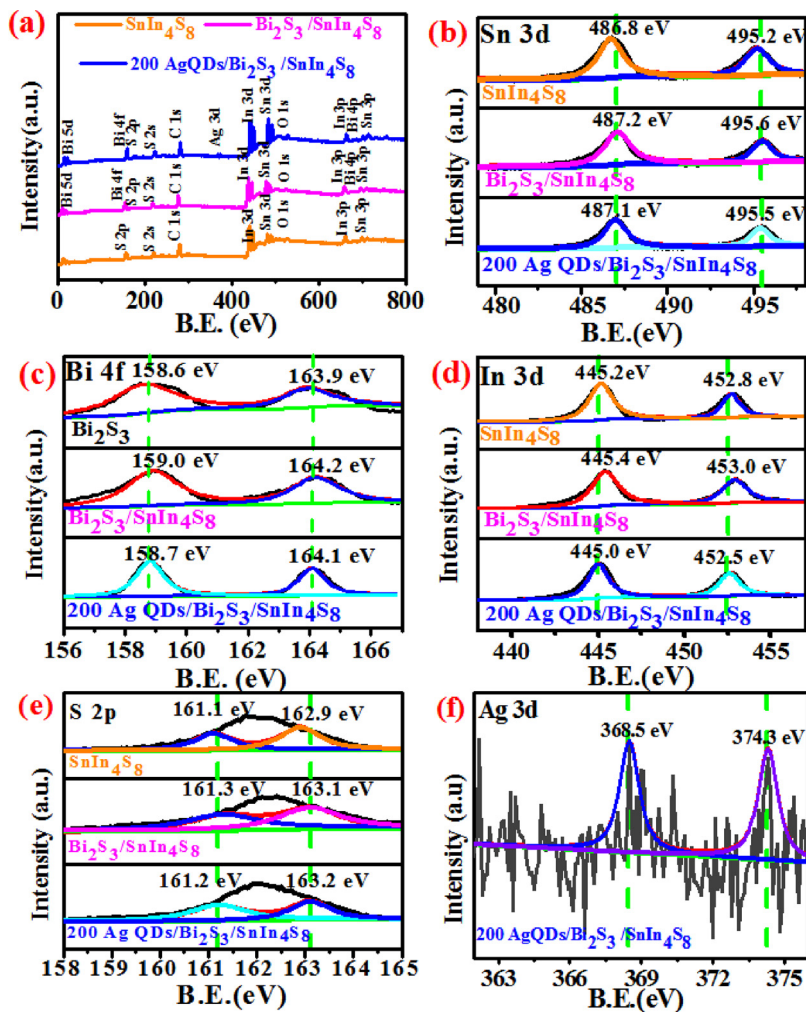


Fig. 3. The XPS spectra of the as-prepared samples (a), Sn 3d (b), Bi 4f (c), In 3d (d), S 2p (e), Ag 3d (f).

exceed load of Ag QDs to reduce the reactive sites.

Considering the fact that Ag release from the containing silver antibacterial material in water disinfection process which may make the contribution to bactericidal through several pathway, such as combine

the thiols of protein enzymes to distorted the metabolism, hinder the replication of DNA by combining with the phosphorus moieties of DNA, promote the permeability and alert the functions of cell membrane by binding to it [39,40]. Here, the Ag release behavior of 200 Ag QDs/

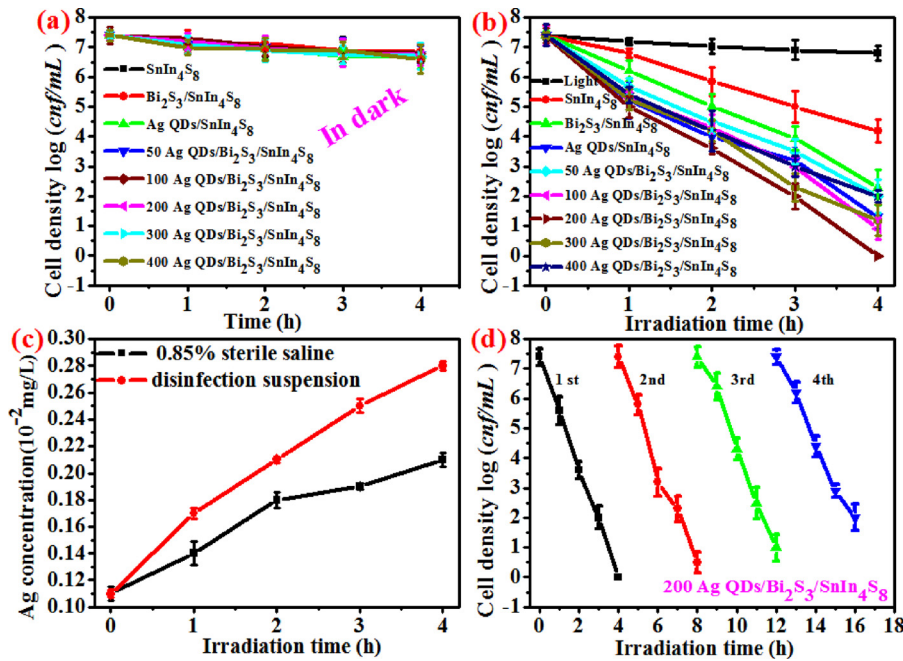


Fig. 4. (a) Cell cytotoxicity of the as-fabricated samples in dark, (b) photodisinfection towards *E. coli* under visible light excitation for each sample ($\lambda > 420$ nm), (c) Ag release concentration of 200 Ag QDs/Bi₂S₃/SnIn₄S₈ in 0.85% sterile saline and disinfection reaction system, (d) cycle experiments of disinfection towards *E. coli* with 200 Ag QDs/Bi₂S₃/SnIn₄S₈ under visible light excitation ($\lambda > 420$ nm). (initial cell density 2.5×10^7 cfu/mL).

Bi₂S₃/SnIn₄S₈ composite in the disinfection suspension and in 0.85% sterile saline were monitored by ICP-MS as shown in Fig. 4c. it can be seen that the Ag release content was gradually increased both in disinfection suspension and sterile 0.85% saline, and the ultimate concentration (0.0028 mg/L) of Ag released in disinfection suspension was higher than that of 0.85% sterile saline(0.0028 mg/L) after 4 h visible light irradiation, illustrating the release of Ag was taken in by cells and trigger the more release of Ag [40]. However, the concentration of release of Ag in our disinfection system was far less than previous reports [41–44], indicating the negligible contribution of antibacterial of Ag in the disinfection process. This could be further verified by the some concentration of released Ag under the same reaction condition: about 0.4-log₁₀ cfu/mL cell loss with 4 h visilbe light irradiation (Fig.S3). On the other hand, the above results demonstrated that the high-efficient inactivation function of the Ag QDs/ Bi₂S₃/SnIn₄S₈ composites was attributed to the photocatalytic reactivation.

3.3. Photodegradation of RhB

RhB was used to further evaluate the photocatalytic property and excavate the potential application of the as-prepared photocatalysts. As shown in Fig. 5a, the RhB almost had not been decomposed in the absence of catalyst, indicating that the effect of visible light on RhB could be neglected. Only 55.79% of RhB was degraded under 20 min visible light irradiation for pure SnIn₄S₈. Comparing to the bare SnIn₄S₈, the Bi₂S₃/SnIn₄S₈ and Ag QDs/SnIn₄S₈ displayed the improved photodegradation efficiency of RhB and the decomposition rate were 70.32% and 88.48%, respectively. Similar to the results of photo-inactivation of *E. coli*, the degradation effect of AgQDs/Bi₂S₃/SnIn₄S₈ composites was firstly up-leaved and subsequently decreased with the increasing mass of Ag QDs introduced to the Bi₂S₃/SnIn₄S₈ system. The 200 AgQDs/Bi₂S₃/SnIn₄S₈ achieved the highest degradation efficiency of RhB which could nearly completely decomposed the RhB within 20 min visible light excitation. The degradation constant (calculated according to fitting the pseudo first-order: $\ln C/C_0 = -kt$) of 200 AgQDs/Bi₂S₃/SnIn₄S₈ was about 3.3-fold and 2-fold of bare SnIn₄S₈ and Bi₂S₃/SnIn₄S₈, respectively (Fig. 5b-c), indicating the Ag QDs/ Bi₂S₃/SnIn₄S₈ composite possess a promising prospect application for organic contaminant decomposition.

Moreover, the adsorptivities of the SnIn₄S₈, Bi₂S₃/SnIn₄S₈, 200 Ag

QDs /Bi₂S₃/SnIn₄S₈ composite was determined by the adsorption of RhB. As shown in Fig. 5d, After the equilibrium was established within 60 min, the adsorption ability of SnIn₄S₈, Bi₂S₃/SnIn₄S₈, Ag QDs/ SnIn₄S₈, 200 Ag QDs/Bi₂S₃/SnIn₄S₈ was 20.01%, 22.13%, 45.07%, 39.84%, respectively. Obviously, the adsorption capacity of Ag QDs/ SnIn₄S₈, 200 Ag QDs/Bi₂S₃/SnIn₄S₈ was significantly improved after the introduction of Ag QDs to SnIn₄S₈ and Bi₂S₃/SnIn₄S₈. This probably attributed to the extreme small size of Ag QDs which enlarged the special surface area (SSA) of the Ag QDs/Bi₂S₃/SnIn₄S₈ composite. Based on the enlarged adsorptivity of 200 Ag QDs/Bi₂S₃/SnIn₄S₈ hybrid, we can conclude that the adsorption played a vital role in the process of photocatalytic system.

3.4. Stability and reusability of photocatalyst

The stability and the reusability of the photocatalyst are the two pivotal factor for the practical application. Here, the photodisinfection towards to *E. coli* with 200 Ag QDs/Bi₂S₃/SnIn₄S₈ hybrid was used to evaluated the stability and the reusability of the samples. As plotted in Fig. 4d, after 4-recycle times disinfection experiments, the photoinactivation ability of 200 Ag QDs/Bi₂S₃/SnIn₄S₈ still maintained high photocatalytic inactivation performance. The reduce deactivation capacity may be attributed to the lost of catalyst in the recollected process, photocorrosion of sulfide photocatalysts, the loss of the Ag after the each recycle and the actives sites were covered by the broken large biomolecules [45–48]. To further demonstrated the stability and reusability of the as-prepared catalyst, the XRD, SEM, EDS and XPS were carried out. As shown in Fig. S4, although slightly corrosion was occurred after four successive used, the main diffraction peaks of Ag QDs/ Bi₂S₃/SnIn₄S₈ still could be observed and no new diffraction peak was appeared (Fig. S5). In Fig. S6, the 200 Ag QDs/Bi₂S₃/SnIn₄S₈ presented flower-like and the EDS images of element Ag, Sn, In, S, Bi still could be observed after four time recycles. Furthermore, the survey XPS (Fig. S7) also revealed that the element Ag, Sn, In, S, Bi were existed in both fresh and reused 200 Ag QDs/Bi₂S₃/SnIn₄S₈ composite. The chemical state of above each element displayed no obviously change after four times recycle (Fig.S7b-f). These results indicated the good stability and reusability of the as-prepared 200 Ag QDs/Bi₂S₃/SnIn₄S₈ composite.

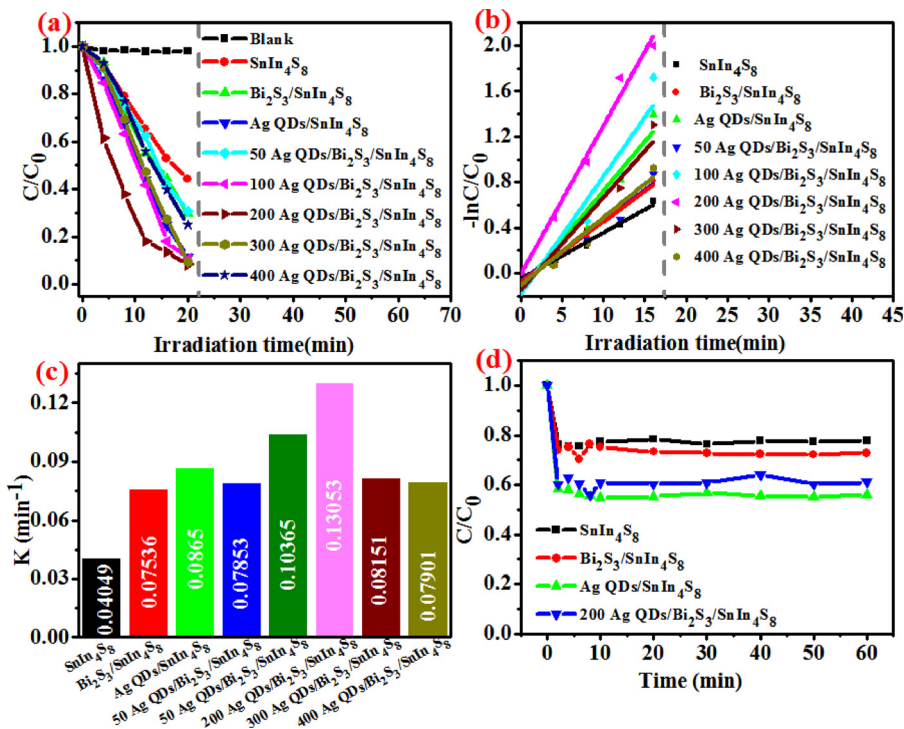


Fig. 5. (a) Photodegradation, (b–c) photodegradation constant (k) and the absorption ability of RhB (10 mg/mL) with as-prepared samples under visible light irradiation ($\lambda > 420 \text{ nm}$).

3.5. Mechanism of photocatalytic disinfection

3.5.1. Cell membrane integrity analysis

It is widely perceived that the death of the bacteria in the photocatalytic process could be attributed to the leakage and damage of cellular content such as to protein and DNA after the cell wall and membrane were disrupted by the photoinduced reactive species hole (h^+), electron (e^-), Superoxide radical (O_2^-) and Hydroxyl radical (OH) [49,50]. Therefore, to illustrate the photocatalytic disinfection mechanism, we firstly observed the morphology change by SEM and fluorescence-based live/dead stain. As shown in Fig. 6, before light irradiation, the cell-membrane was integrity, smooth and presented perfectly rhabdoid shape (Fig. 6a). After 1 h of exposure, the cell began to shrink and depress (Fig. 6b), indicating that the photogenerated reactive species have contact with the out cell membrane of *E. coli*. Remarkably, with the irradiation time evolution, the cell membrane gradually distorted, broken and was completely disrupted after 4 h visible

light excitation (Fig. 6e). The disrupted cell membrane and wall permitted more reactive species entry into the cell to decompose the left cellular content. Moreover, to further reveal the the cell integrity and inactivated *E. coli* by the photocatalysts, the corresponding fluorescence-base live/dead stain with the double AO/EB dyes was carried out. AO can rapidly penetrate the integrity membrane of live cell to combine with DNA and present “green” fluorescence. Adversely, the EB only can pass through the disrupted cell membrane and conjunct with DNA to display “red” fluorescence. As shown in Fig. 6f almost all green fluorescence could be found in the untreated group, indicating the almost all live *E. coli* cells possessed intact cell membrane. After 1 h irradiation, some red fluorescence replaced the green fluorescence (Fig. 6g), suggesting the some of the cell membrane was broken by the reactive species. Obviously, with the irradiation time prolonged, more and more red fluorescence could be found and the green fluorescence nearly absolutely replaced by red fluorescence after 4 h reaction (Fig. 6j), implying the cell membrane was completely disrupted by reactive species

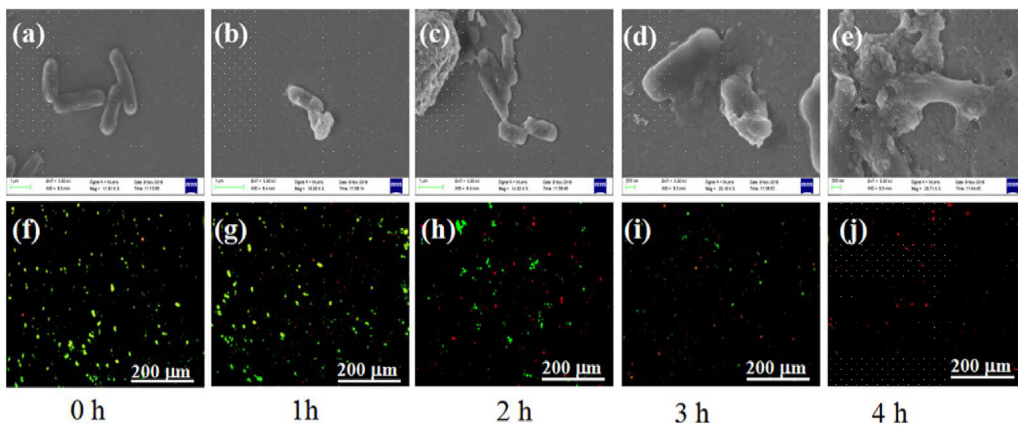


Fig. 6. (a) SEM and (b) live /dead stain of the different times of photoinactivation of *E. coli* with 200 Ag QDs/ $\text{Bi}_2\text{S}_3/\text{SnIn}_4\text{S}_8$ treated. (initial cell density 2.5×10^7 cfu/mL).

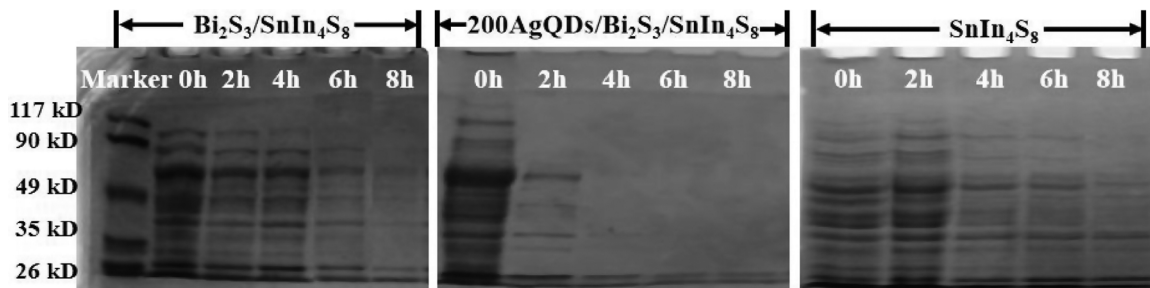


Fig. 7. Expression of total protein of different photodisinfection times by different catalysts (initial cell density 10^8 cfu/mL).

which match well with the result of the morphology change of cell envelope of SEM.

3.5.2. Leakage and decomposition of intracellular biomolecules

The disrupted cell membrane induced by photogenerated reactive species spurred us to deeply investigate the leakage and damage of the pillar components of bacteria: protein and DNA because their crucial role in body metabolism and proliferation [51–53]. The total protein content of *E. coli* was determined with BCA protein Assay Kit (P0010S, Beyotime, Biotech, Shanghai). As Fig. S8 displays, the protein content of 5 mL SnIn_4S_8 cells (10^8 cfu/mL) displayed a certain decrease, from 162.3 to approximately 78.9 $\mu\text{g}/\text{mL}$ after 8 h visible light excitation, which demonstrated that the leakage of the protein during the photocatalytic inactivation process. Apparently, the protein content in 200 Ag QDs/ $\text{Bi}_2\text{S}_3/\text{SnIn}_4\text{S}_8$ group displayed the largest reduction from the 182.3 $\mu\text{g}/\text{mL}$ to 5.2 $\mu\text{g}/\text{mL}$, this may be due to the highest photocatalytic property of 200 Ag QDs/ $\text{Bi}_2\text{S}_3/\text{SnIn}_4\text{S}_8$ which induced the more protein molecules leak out from the broken cell envelop and then oxidized by the photogenerated ROS. To visualize the decomposition of total protein in the inactivation process, the SDS-PAGE was conducted. As depicted in Fig. 7, for the pure SnIn_4S_8 , although the intensity of the protein was gradually fading with the irradiation time evolution, but the reduction trend was not significant which may be due to its limited photocatalytic activity. Contrast to the pure SnIn_4S_8 , the intensity of the protein band were extremely decreased in the $\text{Bi}_2\text{S}_3/\text{SnIn}_4\text{S}_8$ and 200 Ag QDs/ $\text{Bi}_2\text{S}_3/\text{SnIn}_4\text{S}_8$ group, respectively. In particular, the intensity of protein band in the treated with 200 Ag QDs/ $\text{Bi}_2\text{S}_3/\text{SnIn}_4\text{S}_8$ group displayed the largest weak and almost dismissed after 8 h visible light stimulation, coinciding well with its high photocatalytic and the results of BCA test.

The leakage and injury of protein is not the determine factor to the death of bacteria because the self-repair function of the bacteria. Only seriously destroy or loss of the genomic DNA is the final lethal to the cells [51]. Here, AGE was employed to investigate the leakage and damage of DNA in the treated with different catalyst under visible light irradiation. As displayed in Fig. 8, for pure SnIn_4S_8 , the fluorescence intensity of DNA presented negligible fade within 8 h irradiation,

implying very trivial damage of DNA in the inactivated process. Notably, after addition of Bi_2S_3 or Ag QDs, the seriously damage of DNA could be found. In particular, the fluorescence intensity of DNA in the treated with 200 Ag QDs/ $\text{Bi}_2\text{S}_3/\text{SnIn}_4\text{S}_8$ was weaken began at 4 h and nearly absolutely disappeared after 8 h excitation, indicating the seriously distortion of DNA. Based on aforementioned results, we concluded that the death of *E. coli* treated with photocatalyst was attributed to the disruption of cell membrane, leakage and damage of biologic macromolecules such as protein and DNA cause by the photogenerated ROS.

3.5.3. Reactive special analysis

The above results indicated that the death of *E. coli* was mainly induced by the photogenerated ROS. To reveal which reactive species made the dominant contribution to photoactivation of *E. coli* under visible light irradiation ($\lambda > 420 \text{ nm}$). The trapping experiments were carried out with the triethanolamine (TEOA), $\text{K}_2\text{Cr}_2\text{O}_7$, p-benzoquinone (BQ) and isopropanol (IPA) were used as the trapping agent of h^+ , e^- , $\cdot\text{O}_2^-$, $\cdot\text{OH}$, respectively. As shown in Fig. 9a-c, addition of IPA, the inactivated activity of three samples displayed negligible reduction compared with no trapping chemical added, implying the $\cdot\text{OH}$ did not play the leading role in the photodisinfection system. Notably, the photoactivation efficiency was extremely suppressed after addition of triethanolamine (TEOA), p-benzoquinone (BQ) and $\text{K}_2\text{Cr}_2\text{O}_7$ to scavenge the h^+ , $\cdot\text{O}_2^-$, e^- over the three samples. And the identical phenomenon could be also found on degradation of RhB (Fig. S9), suggesting that the e^- , $\cdot\text{O}_2^-$, h^+ played the major role in the photocatalytic bactericidal and degradation. Besides, the intrinsic toxicity of the trapping agents on the viability of *E. coli* cell were also measured in the dark and the results demonstrated their innocuity to the survival of *E. coli* cells (Fig. S10).

To further detect production of $\cdot\text{O}_2^-$ and $\cdot\text{OH}$ in the photo-reaction system. The nitroblue Tetrazolium (NBT) was chosen as the $\cdot\text{O}_2^-$ probe agent because NBT could combine with $\cdot\text{O}_2^-$ to form formazan which could cause decay of the characteristic peak of NBT (259 nm) [54,55]. As displayed in Fig. 10a-c, with the irradiation time evolution, the absorb value of NBT of the three sample was gradually decreased,

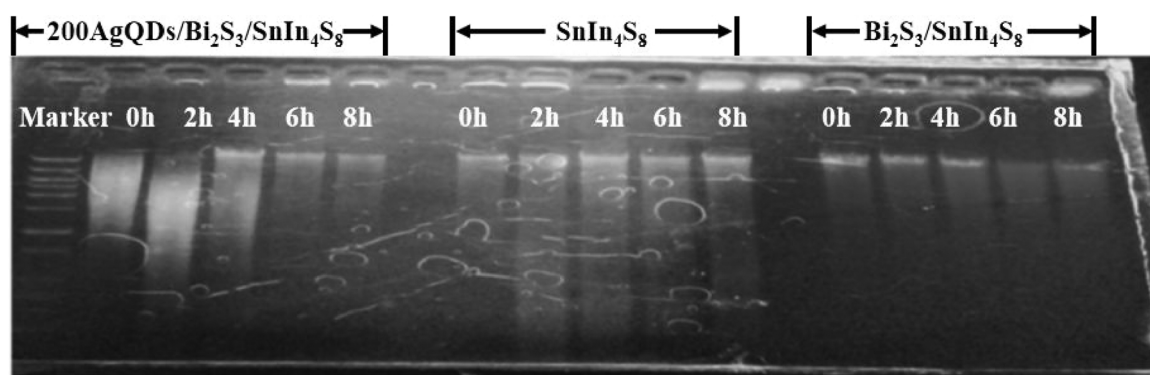


Fig. 8. Expression of DNA of different photodisinfection times with different samples (initial cell density 10^8 cfu/mL).

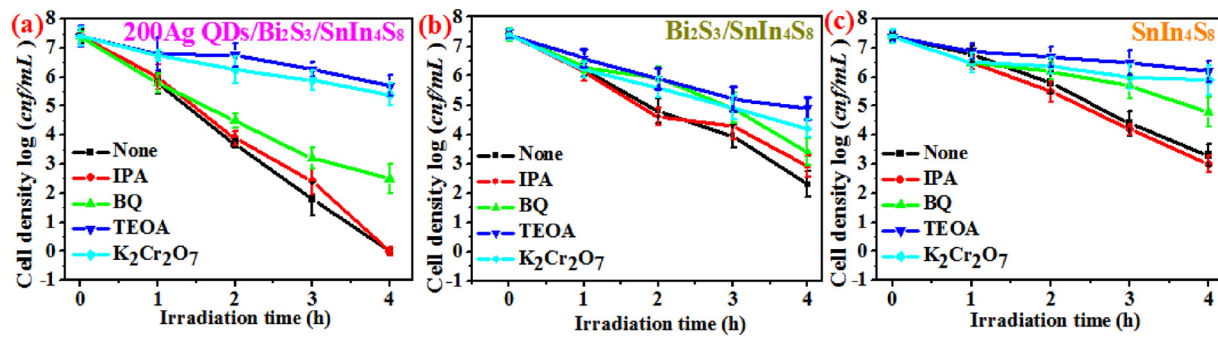


Fig. 9. Photodisinfection ability of SnIn₄S₈, Bi₂S₃/SnIn₄S₈, 200 Ag QDs/Bi₂S₃/SnIn₄S₈ with various trapping agents (initial cell density 10⁷ cfu/mL).

indicating the more and more ·O₂⁻ was generated during the photocatalytic reaction. Besides, the p-phthalic acid (TA) was selected as the probe agent of ·OH for ·OH could combine with TA to form 2-Hydroxyterephthalic acid (TAOH) which possessed 425 distinct peak under 315 nm excitation wavelength [14,56]. As Fig.10d-f displays, there was no signal change could be found at 425 nm after 30 min irradiation, implying no generation of ·OH. The above results further demonstrated that the ·O₂⁻ play the vital role in photocatalytic inactivation and degradation reaction system.

3.6. Mechanism of enhanced photocatalytic property of Ag QDs/Bi₂S₃/SnIn₄S₈ composite

In general, the photocatalytic activity of the photocatalyst was mainly determined by the optical absorption capacity, separation and migration efficiency of photogenerated hole-electron pairs, interface reaction efficiency and specific surface area (SSA). Herein, the UV-vis diffuse reflection spectrum (UV-vis DRS) was employed to analysis the optical property of the samples. As shown in Fig.11a, the pure SnIn₄S₈ possessed the strong light absorb ability below 600 nm. In contrast to SnIn₄S₈, not only the absorb edge of the samples after introducing of Ag QDs or Bi₂S₃ was obviously extended, but also the absorption intensity was clearly enhanced. In particular, the 200 Ag QDs/Bi₂S₃/SnIn₄S₈ displayed the highest light absorption and largest light absorption

region which may attributed to the Local surface plasma resonance (SPR) effect and the enhancement of SnIn₄S₈ surfaced rough degree after the introduction of Ag QDs. Besides, the flower-like morphology of Bi₂S₃/SnIn₄S₈, Ag QDs/Bi₂S₃/SnIn₄S₈ may improve the visible light scatter which may also enhanced the visible light absorption. This property was believed to have positive effect on the photocatalytic activity of the Ag QDs/Bi₂S₃/SnIn₄S₈ composites for more efficient of conversion of solar energy.

Here, The PL was used to investigate the recombination, transfer and separation of photogenerated hole-electron pairs. As shown in Fig. 11b, the PL intensity obeyed the follow order: SnIn₄S₈ > Bi₂S₃/SnIn₄S₈ > Ag QDs/SnIn₄S₈ > 200 Ag QDs/Bi₂S₃/SnIn₄S₈, implying that both the introduction of Ag QDs and Bi₂S₃ could inhibit the recombination of photogenerated charge carries and the Ag QDs made a more negative contribution to the recombination of photogenerated charge carries than that of Bi₂S₃ which may be due to the high trapping electron ability of Ag QDs. Moreover, we can find that the spectra shape of the PL was changed after the Ag QDS were introduced into the Bi₂S₃/SnIn₄S₈, indicating the interaction among the Ag QDS, Bi₂S₃ and SnIn₄S₈.

Photocurrent and EIS were employed to illustrate the separation and diffusion of the photoproduced electron in the catalysts. As show in Fig. 11c, the 200 Ag QDs/Bi₂S₃/SnIn₄S₈ exhibited the highest photocurrent density compared to other samples, indicting the superior

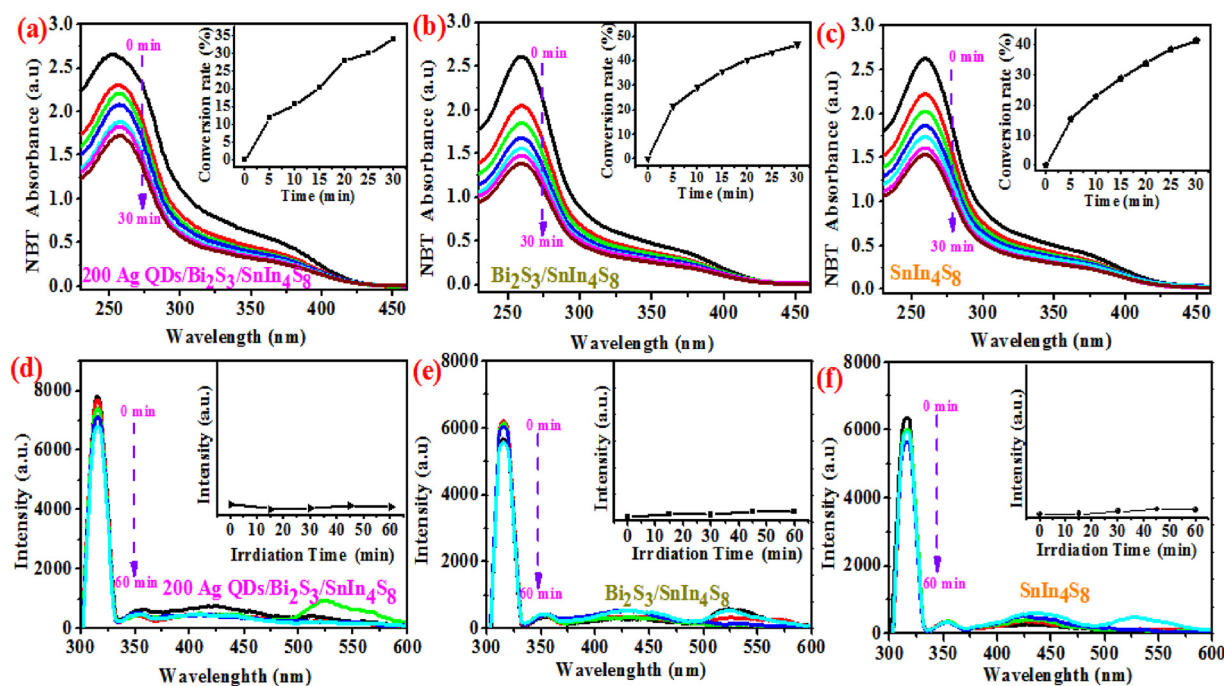


Fig. 10. Detection of ·O₂⁻ and ·OH with NBT (a–c) and TA (d–f) in SnIn₄S₈, Bi₂S₃/SnIn₄S₈, 200 Ag QDs/Bi₂S₃/SnIn₄S₈ hybrid under visible light irradiation.

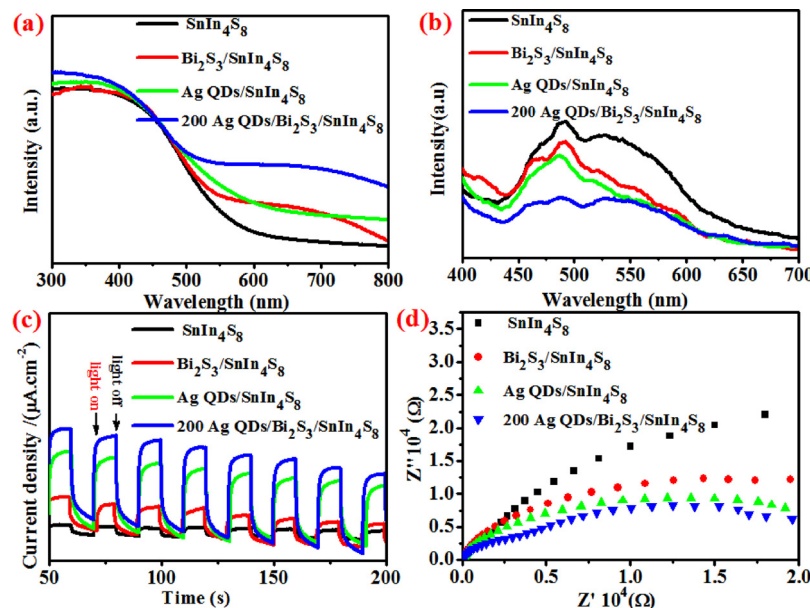


Fig. 11. (a) UV-vis diffuse spectra, (b) photoluminescence (PL) spectra, (c) photocurrent spectra and (d) electrochemical impedance spectrum.

separation and migration efficiency of 200 Ag QDs/Bi₂S₃/SnIn₄S₈. Besides, the results of the EIS further demonstrated that the 200 Ag QDs/Bi₂S₃/SnIn₄S₈ possessed the strongest separation and interface transportation ability of photoexcited hole-electron pairs for its smallest arc radius diameter (Fig. 11d). The enhanced separation and migration efficiency of photoexcited hole electron pairs probably due to the Ag QDs acted as the high-efficient electron sinker.

The BET was applied to analysis the specific surface area and pore size of the SnIn₄S₈, Bi₂S₃/SnIn₄S₈, Ag QDs/SnIn₄S₈, 200Ag QDs/Bi₂S₃/SnIn₄S₈ composite. As Fig. 12a shows, the adsorption-desorption isotherm of above three samples were attributed to the type IV isotherm [57,58], suggesting the slit-like porous structures was developed in the three samples. The BET surface area of SnIn₄S₈ was dramatically enhanced after introducing of Ag QDs or Bi₂S₃ and the surface area of SnIn₄S₈, Bi₂S₃/SnIn₄S₈, Ag QDs/SnIn₄S₈, 200 Ag QDs/Bi₂S₃/SnIn₄S₈ composite were 74.201 m²/g, 99.969 m²/g, 130.592 m²/g, 104.355 m²/g, respectively. Beside, As summarized in table S1 the BJH pore size and pore volume of 200 Ag QDs/Bi₂S₃/SnIn₄S₈ composite were enlarged compared to the pure SnIn₄S₈ and Bi₂S₃/SnIn₄S₈ composite (Fig. 12b). The above results indicated that the introduction of Ag QDs and Bi₂S₃ into the SnIn₄S₈ not only increased the specific surface area, pore size and pore volume of Ag QDs/Bi₂S₃/SnIn₄S₈ composite but also improved its photocatalytic activity by providing more active site and improving the adsorption capacity. All of these results suggested that the Ag QDs played a versatile function in improving the photocatalytic activity of Ag QDs/Bi₂S₃/SnIn₄S₈ composites, such as strengthened the light absorption by SPR effect, acted as electron injector to enhanced the separation and migration of photocatalytic

photoexcited hole-electron pair.

3.7. Transfer model of photogenerated charge carriers

To deeply illustrate the generant redox on the surface of photocatalyst, the band potential alignment were measured with Mott-Schottky plots (MS), Tacus formula and XPS. As Fig.13 (inset, a-b) shows, both SnIn₄S₈ and Bi₂S₃ assigned to the n type semiconductor owing to the positive slope of Mott-Schottky plots and the flat band voltage (E_{fb}) of SnIn₄S₈ and Bi₂S₃ were equal to -0.81 eV and 0.27 eV (vs. SCE) by extrapolating the MS curve to the zero point of E-axis (Fig.13 a-b), respectively. Generally speaking, for n-type semiconductor, the conductor band potential (E_{CB}) of the semiconductor is equal to the numerical value of E_{fb} , therefore, the E_{CB} of SnIn₄S₈ and Bi₂S₃ were -0.57 eV and 0.51 eV vs.NHE (NHE = 0.24 eV + SCE), respectively. Moreover, based on the Tacus formula, the band gap of above two materials were assayed to 2.11 eV and 1.24 eV, respectively (Fig. S11). And the valence band of them were respectively calculated to 1.54 and 1.75 eV by the equation $E_{eg} = E_{VB} - E_{CB}$, which were consistent with the value of XPS valence band spectra (Fig. S12 a-b).

Based on the aforementioned results, the transfer pathway of the photogenerated carries was discussed here. Under the visible light stimulation, both SnIn₄S₈ and the Bi₂S₃ were photoactivated and produced the electron- hole pairs in their VB and CB, respectively. For the conventional double transfer model in Bi₂S₃/SnIn₄S₈ system, the electrons produced in CB of SnIn₄S₈ would easily migrated to the CB of Bi₂S₃, meanwhile, the holes in the VB Bi₂S₃ transfer to the from the VB of Bi₂S₃ to SnIn₄S₈ since the more negative CB voltage and smaller VB

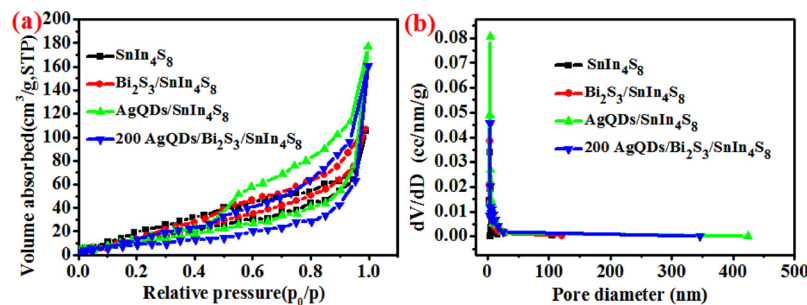


Fig. 12. BET specific surface area (a) and BJH pore size diffusion (b) of SnIn₄S₈ Bi₂S₃/SnIn₄S₈, Ag QDs/SnIn₄S₈, 200 Ag QDs/Bi₂S₃/SnIn₄S₈ composite.

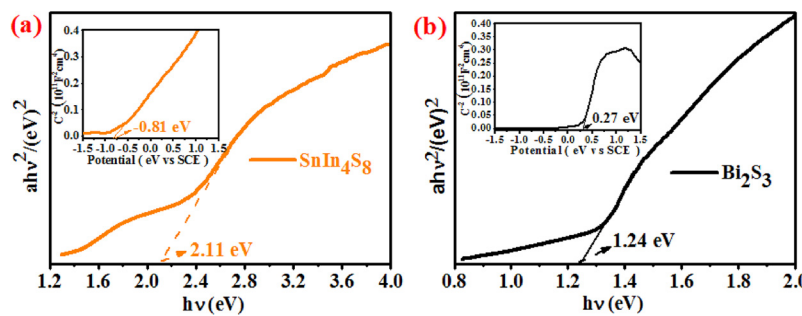


Fig. 13. Tauc's curve (a, b) and Mott-Schottky plots (inset, a, b) of SnIn_4S_8 and Bi_2S_3 .

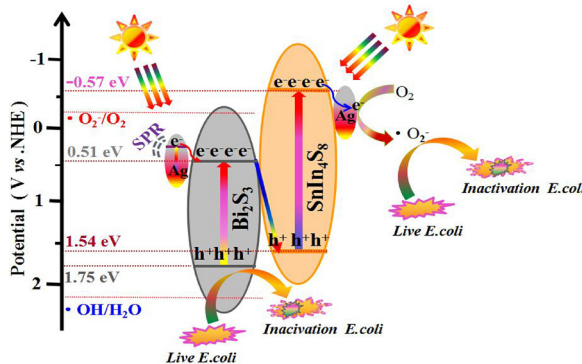


Fig. 14. Photocatalytic disinfection mechanism of Ag QDs/Bi₂S₃/SnIn₄S₈.

voltage of SnIn₄S₈ than that of Bi₂S₃, respectively, which improved the separation rate of photogenerated charge carriers. However, if the photoinduced holes and electrons obeyed this transfer pathway, the ultimate accumulated electrons in the CB of Bi₂S₃ could not reduce the absorbed O₂ molecule to O₂^{·-} due to the more positive VB potential (0.51 eV) than that of reduction potential O₂^{·-} / O₂ (-0.33 eV) [54, 59]. This was contradicted with the results of free radical trapping (Fig. 9) and NBT conversion (Fig. 10) experiments. Consequently, based on above discussions, a plausible traditional Z-Scheme transfer model in Ag QDs/Bi₂S₃/SnIn₄S₈ ternary system (Fig. 14) was proposed. When the Ag QDs/Bi₂S₃/SnIn₄S₈ composite exposed to the visible light, the electrons and holes were generated in the VB and CB of SnIn₄S₈ and the Bi₂S₃, respectively. Afterwards, the electrons generated in the CB of Bi₂S₃ were rapidly migrated to recombine with the holes produced in the VB of SnIn₄S₈. Meanwhile, the high redox power of the electrons and holes accumulated in the CB of SnIn₄S₈ and VB of Bi₂S₃ were still retained there. Thus, the electrons accumulated in the CB of SnIn₄S₈ not only can directly inactivate the bacterial, but also reduce surface absorbed O₂ over the photocatalyst to O₂^{·-} (the E_{CB} of SnIn₄S₈ (-0.47) < E(O₂^{·-} / O₂) = -0.33 eV) which then involved in the photodisinfection process. Moreover, no OH could be generated due to the VB potential of Bi₂S₃ (1.75 eV) was not enough to oxidize H₂O and OH[·] to OH (E(OH[·] / H₂O) = 2.27 eV and (E(OH[·] / OH⁻) = 2.27 eV [58], but the residue holes in the VB of Bi₂S₃ could directly oxidize the cell membrane or biomolecules to induce the definite death of bacteria, which was consistent to the above results of free radical trapping and verification experiments. Moreover, after Ag QDs were introduced into the system, not only the light absorption capacity of catalyst could be improved by the SPR effect, but also Ag could be stimulated to generate electrons which can easily transfer to the CB of Bi₂S₃ since the Fermi level of Bi₂S₃ is higher than that of Ag (+0.14 eV vs. NHE) [32]. Therefore, boost the surface electron stimulation and interfacial electron migration. Furthermore, the Ag QDs also served as the electron sinker to promote the separation and recombination of photoelectrons and reduced the surface absorb O₂ to O₂^{·-} for disinfection [55]. In summary, in the Z-scheme Ag QDs/Bi₂S₃/SnIn₄S₈ system, the synergistic effect of

Ag QDs, Bi₂S₃ and SnIn₄S₈ not only promoted the separation efficiency of photoexcited hole-electron pairs and visible light absorption ability by the SPR effect, but also preserved the high redox ability of holes and electrons for bacteria inactivation, Finally, resulted in the high-efficient photocatalytic disinfection property of Ag QDs/Bi₂S₃/SnIn₄S₈ heterojunction.

3.8. Conclusions

In summary, a novel Ag QDs modified Bi₂S₃/SnIn₄S₈ composite with direct Z-scheme charge carriers transfer model was synthesized through combined with chemical reduction and solvotherm method for high-efficient photodisinfection toward E. coli under visible light stimulation ($\lambda > 420$ nm). The 200 Ag QDs/Bi₂S₃/SnIn₄S₈ hybrid exhibited the strongest deactivation activity of E. coli which can completely deactivate the bacteria with 4 h visible light excitation. The photoinactivation mechanism can be ascribed to the rupture of cell membrane, leakage and damage of intracellular biomolecules. Moreover, the reactive species h⁺, e⁻ and O₂^{·-} play the main role in photodisinfection towards E. coli system. the enhanced photocatalytic activity could be primarily attributed to the promoted visible light absorption capacity, separation and transfer efficiency of photocatalytic charge carriers, enlarged specific surface area induced by the surface plasma resonance (SPR) effect, the electron trapping and injection after Ag QDs was introduced. Furthermore, the Ag QDs/Bi₂S₃/SnIn₄S₈ composite displayed a potential application in organic pollutant removal. this work exhibited a promising environmental friendly substitutable strategy for wastewater purification caused by pathogenic bacteria and organic pollutant.

Acknowledgements

This work was supported by the National Natural Science Foundation of China (Nos. 21476183 and 21676213), the Natural Science Basic Research Plan in Shaanxi Province of China (Nos. 2017JM2026 and 2014JM2-2012), the Ankang Science and Technology Research and Development Plan (2016AK-01-04), and the Scientific Research Project of Shaanxi Education Department (18JK0014).

Appendix A. Supplementary data

Supplementary material related to this article can be found, in the online version, at doi:<https://doi.org/10.1016/j.apcatb.2019.05.020>.

References

- [1] A. Tal, Science, 313 (2006) 1081–1084.
- [2] H. Foster, I. Ditta, S. Varghese, A. Steele, Appl. Microbiol. Biotechnol. 90 (2011) 1847–1868.
- [3] M. Shannon, P. Bohn, M. Elimelech, J. Georgiadis, B. Marinas, A. Mayes, Nature, 452 (2008) 301–310.
- [4] J. Roux, H. Gallard, J. Croué, Environ. Sci. Technol. 46 (2012) 1581–1589.

- [5] S. Hrudey, Water. Res. 43 (2009) 2057–2092.
- [6] M. Tseng, R. Tomada, T. Nakajima, H. Wake, Fems microbiol. Lett. 29 (1985) 211–214.
- [7] D. Tobaldi, C. Piccirillo, R. Pullar, A. Gualtieri, M. Seabra, P. Castro, J. Labrincha, J. Phys. Chem. C 118 (2014) 4751–4766.
- [8] S. Ghafoor, S. Hussain, S. Waseem, S. Arshad, RSC Adv. 8 (2018) 20354–20362.
- [9] B. Liu, Y. Xue, J. Zhang, B. Han, J. Zhang, X. Suo, L. Mu, H. Shi, Environ. Sci: Nano 4 (2017) 255–264.
- [10] J. Li, S. Cai, E. Yu, B. Weng, X. Chen, J. Chen, H. Jia, Y. Xu, Appl. Catal. B: Environ. 233 (2018) 260–271.
- [11] Y. Lei, G. Wang, L. Zhou, W. Hu, S. Song, W. Fan, H. Zhang, Dalton. Trans. 39 (2010) 7021–7024.
- [12] T. Yan, L. Li, G. Li, Y. Wang, W. Hu, X. Guan, J. Hazard. Mater. 186 (2011) 272–279.
- [13] F. Deng, F. Zhong, D. Lin, L. Zhao, Y. Liu, J. Huang, X. Luo, S. Luo, D. Dionysiou, Appl. Catal. B: Environ. 219 (2017) 163–172.
- [14] H. Shi, Y. Zhao, J. Fan, Z. Tang, Appl. Surf. Sci. 465 (2019) 212–222.
- [15] L. Wang, X. Li, W. Teng, Q. Zhao, Y. Shi, R. Yue, Y. Chen, J. Hazard. Mater. 244–245 (2013) 681–688.
- [16] J. Di, J. Xia, M. Ji, B. Wang, S. Yin, Y. Huang, Z. Chen, H. Li, Appl. Catal. B: Environ. 188 (2016) 376–387.
- [17] A. Booshehri, S. Chun-Kiat Goh, J. Hong, R. Jiang, R. Xu, J. Mater. Chem. A 2 (2014) 6209–6217.
- [18] Y. Oaki, K. Sato, J. Mater. Chem. A 6 (2018) 23197–23219.
- [19] T. Salim, S. Sun, Y. Abe, A. Krishna, A. Grimsdale, Y. Lam, J. Mater. Chem. A 3 (2015) 8943–8969.
- [20] L. Ye, J. Liu, C. Gong, L. Tian, T. Peng, L. Zan, ACS Catal. 2 (2012) 1677–1683.
- [21] J. Xu, Z. Gao, K. Han, Y. Liu, Y. Song, ACS Appl. Mater. Interface 6 (2014) 15122–15131.
- [22] S. Abbas, M. Kumar, H. Kim, J. Kim, J. Lee, ACS Appl. Mater. Interface 10 (2018) 14292–14298.
- [23] Q. Wang, T. Hisatomi, Y. Suzuki, Z. Pan, J. Seo, M. Katayama, T. Minegishi, H. Nishiyama, T. Takata, K. Seki, A. Kudo, T. Yamada, K. Domen, J. Am. Chem. Soc. 139 (2017) 1675–1683.
- [24] D. Xia, W. Wang, R. Yin, Z. Jiang, T. An, G. Li, H. Zhao, P. Wong, Appl. Catal. B: Environ. 214 (2017) 23–33.
- [25] L. Zhu, H. Li, P. Xia, Z. Liu, D. Xiong, ACS Appl. Mater. Interface 10 (2018) 39679–39687.
- [26] K. Maeda, ACS Catal. 3 (2013) 1486–1503.
- [27] H. Li, Y. Gao, Y. Zhou, F. Fan, Q. Han, Q. Xu, X. Wang, M. Xiao, C. Li, Z. Zou, Nano. Lett. 16 (2016) 5547–5552.
- [28] Y. Zhu, Z. Chen, T. Gao, Q. Huang, F. Niu, L. Qin, P. Tang, Y. Huang, Z. Sha, Y. Wang, Appl. Catal. B: Environ. 163 (2015) 16–22.
- [29] Z. Chen, F. Bing, Q. Liu, Z. Zhang, X. Fang, J. Mater. Chem. A 3 (2015) 4652–4658.
- [30] F. Chen, Q. Yang, Y. Wang, J. Zhao, D. Wang, X. Li, Z. Guo, H. Wang, Y. Deng, C. Niu, G. Zeng, Appl. Catal. B: Environ. 205 (2017) 133–147.
- [31] H. Zhou, Z. Wen, J. Liu, J. Ke, X. Duan, S. Wang, Appl. Catal. B: Environ. 242 (2019) 76–84.
- [32] Z. Wang, X. Xu, Z. Si, L. Liu, Y. Liu, Y. He, R. Ran, D. Weng, Appl. Surf. Sci. 450 (2018) 441–450.
- [33] Z. Zhu, Z. Lu, D. Wang, X. Tang, Y. Yan, W. Shi, Y. Wang, N. Gao, X. Yao, H. Dong, Appl. Catal. B: Environ. 182 (2016) 115–122.
- [34] Y. Zhang, Z. Du, K. Li, M. Zhang, D. Dionysiou, ACS Appl. Mater. Interface 3 (2011) 1528–1537.
- [35] X. Qiao, Z. Zhang, Q. Li, D. Hou, Q. Zhang, J. Zhang, D. Li, P. Feng, X. Bu, J. Mater. Chem: A 6 (2018) 22580–22589.
- [36] Y. Deng, L. Tang, G. Zeng, C. Feng, H. Dong, J. Wang, H. Feng, Y. Liu, Y. Zhou, Y. Pang, Environ. Sci: Nano 4 (2017) 1494–1511.
- [37] X. Yuan, L. Jiang, X. Chen, L. Leng, H. Wang, Z. Wu, T. Xiong, J. Liang, G. Zeng, Environ. Sci: Nano 4 (2017) 2175–2185.
- [38] L. Stabryla, K. Johnston, J. Millstone, L. Gilbertson, Environ. Sci: Nano 5 (2018) 2047–2068.
- [39] D. Xia, T. An, G. Li, W. Wang, H. Zhao, P. Wong, Water. Res. 99 (2016) 149–161.
- [40] N. Wigginton, A. Titta, F. Piccapietra, J. Dobias, V. Nesatyy, M. Suter, R. Latmani, Environ. Sci. Technol. 44 (2010) 2163–2168.
- [41] G. Xiao, X. Zhang, W. Zhang, S. Zhang, H. Su, T. Tan, Appl. Catal. B: Environ. 170–171 (2015) 255–262.
- [42] X. Xie, C. Mao, X. Liu, L. Tan, Z. Cui, X. Yang, S. Zhu, Z. Li, X. Yuan, Y. Zheng, K. Yeung, P. Chu, S. Wu, ACS Cent. Sci. 4 (2018) 724–738.
- [43] Q. Zhou, S. Ma, S. Zhan, Appl. Catal. B: Environ. 224 (2018) 27–37.
- [44] A. Helal, F. Harraz, A. Ismail, T. Sami, I. Ibrahim, Appl. Catal. B: Environ. 213 (2017) 18–27.
- [45] D. Xia, T. An, G. Li, W. Wang, H. Zhao, P. Wong, Water. Res. 99 (2016) 149–161.
- [46] T. Yan, J. Tian, W. Guan, Z. Qiao, W. Li, J. You, B. Huang, Appl. Catal. B: Environ. 202 (2017) 84–94.
- [47] Y. Xie, Y. Zheng, Y. Yang, R. Jiang, G. Wang, Y. Zhang, E. Zhang, L. Zhao, C. Duan, J. Colloid. Interface Sci. 514 (2018) 634–641.
- [48] Y. Feng, L. Liu, J. Zhang, H. Aslan, M. Dong, J. Mater. Chem. B. 5 (2017) 8631–8652.
- [49] W. Wang, G. Li, D. Xia, T. An, H. Zhao, P. Wong, Photocatalytic nanomaterials for solar-driven bacterial inactivation: recent progress and challenges, Environ. Sci: Nano 4 (2017) 782–799.
- [50] D. Xia, Z. Shen, G. Huang, W. Wang, J. Yu, P. Wong, Environ. Sci. Technol. 49 (2015) 6264–6273.
- [51] H. Sun, G. Li, X. Nie, H. Shi, P.K. Wong, H. Zhao, T. An, Environ. Sci. Technol. 48 (2014) 9412–9419.
- [52] T. Leung, C. Chan, C. Hu, J. Yu, P. Wong, Water. Res. 42 (2008) 4827–4837.
- [53] Y. Zhao, X. Liang, H. Shi, Y. Wang, Y. Ren, E. Liu, X. Zhang, J. Fan, X. Hu, Chem. Eng. J. 353 (2018) 56–68.
- [54] J. Wan, X. Du, E. Liu, Y. Hu, J. Fan, X. Hu, J. Catal. 345 (2017) 281–294.
- [55] Hirakawa T, Y. Nosaka, Langmuir 18 (2002) 3247–3254.
- [56] S. Wang, B. Zhu, M. Liu, L. Zhang, J. Yu, M. Zhou, Appl. Catal. B: Environ. 243 (2019) 19–26.
- [57] W. Zhao, Y. Liu, Z. Wei, S. Yang, H. He, C. Sun, Appl. Catal. B: Environ. 185 (2016) 242–252.
- [58] J. Li, Y. Yin, E. Liu, Y. Ma, J. Wan, J. Fan, X. Hu, J. Hazard. Mater. 321 (2017) 183–192.